

# Structural transformations in porous glasses under mechanical loading. II. Compression

Nikolai V. Priezjev<sup>1,2</sup> and Maxim A. Makeev<sup>3</sup>

<sup>1</sup>*Department of Mechanical and Materials Engineering,*

*Wright State University, Dayton, OH 45435*

<sup>2</sup>*National Research University Higher School of Economics, Moscow 101000, Russia and*

<sup>3</sup>*Department of Chemistry, University of Missouri-Columbia, Columbia, MO 65211*

(Dated: February 2, 2022)

## Abstract

The role of porous structure and glass density in response to compressive deformation of amorphous materials is investigated via molecular dynamics simulations. The disordered, porous structures were prepared by quenching a high-temperature binary mixture below the glass transition into the phase coexistence region. With decreasing average glass density, the pore morphology in quiescent samples varies from a random distribution of compact voids to a porous network embedded in a continuous glass phase. We find that during compressive loading at constant volume, the porous structure is linearly transformed in the elastic regime and the elastic modulus follows a power-law increase as a function of the average glass density. Upon further compression, pores deform significantly and coalesce into large voids leading to formation of domains with nearly homogeneous glass phase, which provides an enhanced resistance to deformation at high strain.

PACS numbers: 34.20.Cf, 68.35.Ct, 81.05.Kf, 83.10.Rs

## I. INTRODUCTION

The prediction of the mechanical response of disordered solids is important for a number of industrial applications, and, at the same time, it poses a challenging fundamental problem [1, 2]. It is well recognized by now that deformation and flow of bulk metallic glasses occur via rapid localized rearrangements of atoms that induce strongly anisotropic stress redistribution over long distances [3, 4]. At the mesoscopic level, this process can be described by elastoplastic models, where the system is coarse-grained into interacting elements that obey a set of rules including linear elastic response, local yield criterion, stress propagation, and recovery [1]. Interestingly, atomistic simulations revealed that both the yield and flow stresses of metallic glasses [5] and nanocrystalline metals [6] are higher in compression than in tension. More recently, it was shown that several factors affect deformation and failure of cellular metallic glasses under compression; namely, the cell size controls the transition from localized to homogeneous plastic deformation, while the cell shape, e.g., circular versus hexagonal, might change the strength and energy absorption capacity due to variation in stress concentration at the cell surface [7]. Nevertheless, a complete understanding of the elastic response and yield in homogeneous and porous metallic glasses is yet to be achieved.

A number of recent experimental studies have reported the results of uniaxial compression tests performed on metallic glass pillars [8–14]. Most importantly, it was found that when the sample size is decreased down to the submicron dimensions, the deformation mode changes from shear band propagation to homogeneous plastic flow, which can be attributed to the existence of a critical strained volume required for the formation of a shear band [9]. The observed behavior can be rationalized by realizing that collectivity of flow defects, or shear transformation zones, toward localization is suppressed in sufficiently small systems, and the enhanced ductility corresponds to a large number of weakly correlated shear transformations [8]. It was also shown that during compression of micron-scale amorphous silica pillars, the plastic deformation is accompanied with a periodic array of radial cracks at the top of the pillars, which results in some case in splitting into two parts upon unloading [15]. However, despite significant efforts, the correlation between ductility, fracture, and strength of amorphous materials as well as the dependence on preparation history and loading conditions remain not fully understood to date.

The microscopic mechanisms of the glass-gas phase separation kinetics at constant volume

were recently studied using molecular dynamics simulations [16, 17]. Following a rapid quench below the glass transition temperature, a simple glass-forming system was found to gradually transform into an amorphous solid with a porous structure whose properties depend strongly on the average glass density and temperature [16, 17]. Interestingly, it was shown that the pore-size distribution functions obey a single scaling relation at small length scales for systems with high porosity, while the local density of the solid phase remains relatively insensitive to the total pore volume [18]. Later studies have examined the dynamic response of porous glasses subjected to either steady shear [19] or tensile [20] deformation. In both cases it was found that the porous structure becomes significantly modified due to pore redistribution and coalescence into large voids upon increasing strain [19, 20]. The analysis of local density profiles during tensile loading showed that necking develops in the low-density regions leading to an extended plastic strain and ultimate breaking of the material [20].

In our recent study [19], we discussed the theoretical models, developed to describe the elastic moduli of porous materials and compared our simulation results on shear deformation of porous glasses with analytical predictions. We found that the simulated modulus dependence on density can not be described using a single theory. However, the data can be fitted in the limits of low and high porosities using different approaches (see [19] and references therein). In the limit of large porosities, the percolation theory was found to adequately describe the simulation data. In the limit of low porosities, a model, based on the Eshelby approach to the problem of embedded inclusions, can be utilized. The general conclusion of the study [19] is that elastic response properties of porous materials are strongly dependent on the particular realization of pore-size distribution and topology of pore network in the sample. Recently, similar conclusions were reached by the authors of Ref. [21], who pointed out the existing differences between materials with isolated pores and those having more complicated topology of porous structures.

In this study, we examine the evolution of porous structure and mechanical response of amorphous solids subjected to compressive loading using molecular dynamics simulations. It will be shown that after an isochoric quench to a temperature below the glass transition, a variety of pore morphologies are formed, including a random distribution of isolated voids or a connected porous network, upon reducing average glass density. We demonstrate that

under compressive loading, the porous structure is gradually transformed via pore coalescence and void redistribution out of the glass phase, which results in nearly uniform density profiles at high strain.

The paper is organized as follows. The next section contains the details of molecular dynamics simulation model and the deformation procedure. Results of the numerical analysis of pore size distributions, local density profiles, and mechanical properties of porous glasses are presented in Sec. III. The conclusions are given in the last section.

## II. SIMULATION DETAILS

In this study, the deformation and structure of porous glassy systems were investigated using the Kob-Andersen (KA) binary mixture (80:20) model at a low temperature [22]. In the KA model, the pairwise interaction between atoms  $\alpha, \beta = A, B$  is described via the truncated Lennard-Jones (LJ) potential

$$V_{\alpha\beta}(r) = 4\varepsilon_{\alpha\beta} \left[ \left( \frac{\sigma_{\alpha\beta}}{r} \right)^{12} - \left( \frac{\sigma_{\alpha\beta}}{r} \right)^6 \right], \quad (1)$$

with the non-additive interaction parameters  $\varepsilon_{AA} = 1.0$ ,  $\varepsilon_{AB} = 1.5$ ,  $\varepsilon_{BB} = 0.5$ ,  $\sigma_{AB} = 0.8$ , and  $\sigma_{BB} = 0.88$  [22]. The mass of atoms of types  $A$  and  $B$  is the same, i.e.,  $m_A = m_B$ . The cutoff radius is taken to be  $r_{c,\alpha\beta} = 2.5\sigma_{\alpha\beta}$  to improve computational efficiency. The reduced units of length, mass, energy, and time are defined as follows  $\sigma = \sigma_{AA}$ ,  $m = m_A$ ,  $\varepsilon = \varepsilon_{AA}$ , and  $\tau = \sigma\sqrt{m/\varepsilon}$ , respectively. The Newton's equations of motion were integrated using the velocity-Verlet algorithm [23, 24] with the time step  $\Delta t_{MD} = 0.005\tau$ . The total number of atoms is  $N = 300\,000$ . All molecular dynamics simulations were performed using the LAMMPS numerical code, which is designed to run efficiently in parallel using the domain-decomposition method [23].

Following the preparation protocol used in the previous studies [16–20], the system was first equilibrated at constant volume during  $3 \times 10^4 \tau$ . At this stage, the temperature of  $1.5\varepsilon/k_B$ , where  $k_B$  is the Boltzmann constant, was maintained by velocity rescaling. At this temperature the binary mixture is in the liquid phase. To remind, the glass transition temperature of the KA model is  $T_g \approx 0.435\varepsilon/k_B$  [22]. The second step involves an instantaneous quench of the system to the target temperature of  $0.05\varepsilon/k_B$  and subsequent evolution of the system during an additional time interval of  $10^4 \tau$  at constant volume. As a result of



concurrent phase separation and solidification at the low temperature, an amorphous solid with a complex porous structure is formed, as shown, for example, in Fig. 1 for the average glass densities  $\rho\sigma^3 = 0.2, 0.4, 0.6$  and  $0.8$ . In the present study, the MD simulations were carried out in a wide range of average glass densities,  $0.2 \leq \rho\sigma^3 \leq 1.0$ , and five independent samples.

The compression deformation was conducted on porous glasses along the  $\hat{x}$  direction with the strain rate  $\dot{\varepsilon}_{xx} = 10^{-4} \tau^{-1}$  at constant volume. The maximum compressive strain is 80 %, which means that the cell size in the  $\hat{x}$  direction is reduced from  $L_x$  to  $0.2 L_x$  at the maximum strain. As in quiescent samples, the temperature of  $0.05 \varepsilon/k_B$  was maintained via the Nosé-Hoover thermostat [23]. During compressive deformation, the stress tensor, potential energy, and system size were saved every  $0.5 \tau$  for the postprocessing analysis, which was supplemented by visual examination of consecutive atomic configurations. The data for the elastic modulus were averaged over five independent realizations of disorder, while representative snapshots and locally averaged density profiles as well as pore size distributions are reported for one sample at a given average glass density.

### III. RESULTS

The process of phase separation and concurrent solidification of a glass-forming fluid at constant volume leads to formation of complex porous structures in an amorphous solid [16, 17]. With increasing average glass density, a number of distinct morphologies were reported at temperatures below the glass transition; namely, disconnected droplets of the dense phase, bicontinuous structures with increasing fraction of the solid phase, and randomly distributed isolated pores inside the amorphous solid [16, 17]. Typical atomic configurations of quiescent glassy systems considered in the present study are shown in Fig. 1 for the average glass densities  $\rho\sigma^3 = 0.2, 0.4, 0.6$  and  $0.8$ . Note that pore connectivity increases in samples with lower average glass densities, while the structure of the solid domains remains continuous. In our previous study, it was demonstrated that the distribution of pore sizes in the absence of deformation is well described by a scaling relation at small length scales and the average glass density  $\rho\sigma^3 \lesssim 0.8$  [18].

Figure 2 shows the stress-strain curves measured in one sample for each value of the average glass density  $\rho\sigma^3 \in [0.2, 1.0]$ . For completeness, the data for both compression

( $\varepsilon_{xx} < 0$ ) and tension ( $\varepsilon_{xx} > 0$ ) deformations are reported. Notably, the zero strain values of stress  $\sigma_{xx}$  are finite due to the negative pressure, which arises as a result of thermal quench to the low temperature of  $0.05 \varepsilon/k_B$  at constant volume [18, 20]. Notice that the elastic range extends up to  $|\varepsilon_{xx}| \lesssim 0.04$ , which is followed by the plastic regime of deformation until the maximum strain  $|\varepsilon_{xx}| = 0.8$ . The elastic modulus was computed from the slope of compressive stress  $\sigma_{xx}(\varepsilon_{xx})$  at  $|\varepsilon_{xx}| \leq 0.01$  and averaged over five independent samples. In agreement with our previous studies [18, 20], the variation of the elastic modulus as a function of the average glass density follows a power-law increase with the exponent of 2.41 (see inset to Fig. 2). Under compressive loading, the stress is first reduced to zero and then becomes negative, which indicates that nearly homogeneous glass phase is accumulated in some parts of highly strained samples, thus, providing resistance to deformation. This effect is illustrated in consecutive systems snapshots upon increasing strain (see Figs. 3–5). In turn, the pore deformation morphologies are more clearly visualized in narrow slices across the systems shown in Figs. 6–8 for the average glass densities  $\rho\sigma^3 = 0.3, 0.5$  and  $0.8$ .

In this work, the pore size distribution (PSD) functions are obtained using the open-source software ZEO++ [25–27]. The approach is based upon a Voronoi network representation of the accessible void space. Specifically, Voronoi network consists of nodes and edges mapping the space around atoms in the system. Each node and edge contain information on the distances to the nearest atoms; the distances correspond to the radii of the *largest* probe of a spherical shape that can move along the edge without intersecting any atom. The probe-accessible regions are found via the modified Dijkstra shortest-path algorithm [28]. Within this framework, the probe-accessible regions of the periodic Voronoi network are represented by a sub-graph. Thereby, an atomic structure can be converted into a periodic graph-representation of the void space for a given radius of the probe.

The pore size distribution functions,  $\Phi(d_p)$ , are shown in Fig. 9. Here, we present our results for the cases of average densities  $\rho\sigma^3 = 0.3, 0.5$  and  $0.8$ . The PSD functions in quiescent samples for the same set of  $\rho\sigma^3$  values have been studied in Ref. [18]. It was shown that PSDs are narrow at high glass densities and they become broader as the average glass density decreases; various features of PSDs were discussed in the same reference. In the past, we have also investigated evolutions of PSDs in porous glasses undergoing shear [19] and tensile [20] loadings. This allows for a comparative analysis of the data, obtained on

different types of mechanical loading.

First, we found that the general behavior of the PSDs under compression is similar to the cases of shearing and tension at small and intermediate strain deformation. Indeed, when strain is small, the shape of PSD curves shown in Fig. 9 remains largely unaffected, and the widening of the PSDs is small. With increasing strain, the PSDs widen significantly and gradually start to develop a double-peak profile. The same type of behavior has been observed in the systems undergoing structural evolution under shear and tension [19, 20]. In the cases under consideration, the magnitudes of PSDs decrease drastically with strain in the regions of small values of  $d_p$ . At the same time, the magnitudes of peaks, newly developed at large values of  $d_p$ , increase (see Fig. 9). This is consistent with the results reported for porous glasses under shear and tension [19, 20]. However, compression above the threshold value of  $\approx 0.7$  leads to a nearly complete separation of the porous glass into solid domain and void space. At densities  $\rho\sigma^3 = 0.3$  and  $0.5$ , the separation leads to a formation of the void space region with linear dimension exceeding that of a half of the system size in the direction perpendicular to the loading axis. According to our analysis, a substantial densification takes place in the solid domains, with the maximum of the density profile along the  $\hat{y}$  direction being more than twice the average density of the system (not shown).

Second, previously we found that, in the case of tension, the system with density  $\rho\sigma^3 = 0.8$  shows anomalously large peak, corresponding to large-size pore developed in the system [20]. Here, again, the same type of behavior is observed. The system undergoes a rapid separation into high-density solid material (glass) and large voids. Note that the finite-size effects may interfere with the process of void growth, when a pore diameter becomes close the system's characteristic dimension. Therefore, one should exercise some caution in interpreting the data, when dimensions of the pores approach those of the simulation box. The growth of large-size voids is accompanied by significant decrease in the number of pores having dimension characteristic for unperturbed samples. Indeed, the small-size pores nearly disappear, when  $\varepsilon_{xx}$  exceeds  $0.5$  in the system with  $\rho\sigma^3 = 0.8$  shown in Fig. 9. Altogether, the general conclusions are similar to the cases of shearing and tension [19, 20]. Those can be summarized as follows. Compressive deformation leads to multiple structural transitions, characterized by gradual evolution from a number of small-size compact pores to a configuration with one

or two dominant pores.

A temporal picture of material rearrangement under compression can be unveiled by considering spatially-resolved (coarse-grained) density profiles at a chosen sets of compressive strain magnitudes. Similar to our study of porous glass response to tension [20], here we consider spatially-resolved average density, computed along the direction of compressive loading,  $\langle \rho \rangle_s(x)$ . The quantity is defined as the number of atoms located in a bin with thickness  $b \approx \sigma$  along the  $\hat{x}$  direction (the direction of the loading), divided by the volume of the bin:  $b L_y L_z$ , where,  $L_y$  and  $L_z$  are the box sizes in the two Cartesian directions perpendicular to the loading direction. In Ref. [20], we found that the failure under tension occurs in large-scale, low-density regions. In other words, the location of the failure is correlated to the low-density regions of large spatial extents [20].

As shown below, in the case of compressive loading, there also exists a number of notable events pertained to the structural evolution. Correspondingly, in Figs. 10–12, we mark the low-density regions by dashed vertical lines. As follows from Figs. 10–12, two different types of behavior can be discriminated depending on the average density of porous glasses. Next, we consider the two types separately. In the low- and intermediate-density systems ( $\rho\sigma^3 = 0.3$  and  $0.5$ ), the compression induces a densification of the regions with initially low local densities, while the density shows some decrease in the domains, where  $\rho\sigma^3$  was above the average value before loading. In a sense, the effect can be described as a gradual rearrangement of the glassy material, such that the local density along the direction of compression is homogeneous and equals to the average density. This behavior is characteristic for small and intermediate values of compressive strains. As the strain magnitude approaches  $\varepsilon_{xx} = 0.7$ , an abrupt homogenization occurs, with the average density rapidly approaching the average value, i.e.,  $\rho\sigma^3 = 0.3$  and  $0.5$  (see Figs. 10 and 11).

The behavior is markedly different for systems with  $\rho\sigma^3 = 0.8$  shown in Fig. 12. In this case, the zone of low-density (marked by vertical dashed lines) does not undergo densification. To the contrary, a density dip develops within the zone, moves towards one border of the low-density zone and gets localized at this border at intermediate values of  $\varepsilon_{xx}$ . At high strain magnitudes, an apparent pore closures take place in the whole sample, the density is close to homogeneous, and its value approaches the average density,  $\rho\sigma^3 = 0.8$ . We would like to reiterate that the porous glasses in our study were formed in confined environment.

Correspondingly, we perform the compressive loading tests at constant volume. Therefore, the systems are different from the seemingly equivalent set-ups, widely used in the studies of shock-wave propagation through porous media. In the case of shock-wave propagation, a density increase in the after-shock regions takes place, with the shocked material density being in excess of its thermodynamic equilibrium value [29–32]. In the case, considered herein, we rather observe a nearly complete separation of bimodal systems in solid domains and void, with density of these solid domains gradually approaching its equilibrium value for the void-free state ( $\rho\sigma^3 = 1.25$  [33]). Since the volume is conserved (unlike the case of shock-compression), the average density approaches its corresponding value throughout the samples. The systems we consider can be of relevance to the problems related to gas absorption or flow of gas (fluid) in nano-porous materials, where stresses can arise, for example, from adsorbates [34]. The problem of shock-waves in the system under consideration will be addressed in a future work.

#### IV. CONCLUSIONS

In summary, we reported the results of a molecular dynamics study aimed at understanding the influence of pore and glass structures on compressive loading at constant volume and low temperature. For a given average glass density, the porous samples were produced at constant volume through kinetically arrested liquid-gas spinodal decomposition of a glass-forming system at a temperature well below the glass transition. The resulting structures are characterized by a connected porous network at lower average glass densities and a collection of randomly distributed compact pores at higher average glass densities. In addition, in a wide range of average glass densities, the pressure in quiescent samples is negative due to a distribution of built-in tensile stresses in the solid domains. We found that upon compressive loading, the axial stress is first reduced to zero, thus releasing built-in stresses in the system, and then it becomes negative due to accumulation of the homogeneous glass at high strain. In agreement with our previous results on tensile and shear deformation, the compressive elastic modulus increases as a power-law function of the average glass density. Finally, the numerical analysis of density profiles and pore size distributions during compressive loading showed that porous structures undergo significant deformation and expulsion from the glass phase leading to effective separation of empty regions from the homogeneous solid domains.

## Acknowledgments

Financial support from the National Science Foundation (CNS-1531923) is gratefully acknowledged. The molecular dynamics simulations were performed using the LAMMPS numerical code developed at Sandia National Laboratories [23]. The study has been in part funded by the Russian Academic Excellence Project ‘5-100’. Computational work in support of this research was performed at Michigan State University’s High Performance Computing Facility and the Ohio Supercomputer Center.

- 
- [1] A. Nicolas, E. E. Ferrero, K. Martens, J.-L. Barrat, Deformation and flow of amorphous solids: a review of mesoscale elastoplastic models, review article (2017). (arXiv:1708.09194).
  - [2] Z. D. Sha, W. H. Wong, Q. X. Pei, P. S. Branicio, Z. S. Liu, T. J. Wang, T. F. Guo, H. J. Gao, Atomistic origin of size effects in fatigue behavior of metallic glasses, *J. Mech. Phys. Solids*, **104**, 84 (2017).
  - [3] A. S. Argon, Plastic deformation in metallic glasses, *Acta Metall.* **27**, 47 (1979).
  - [4] F. Spaepen, A microscopic mechanism for steady state inhomogeneous flow in metallic glasses, *Acta Metall.* **25**, 407 (1977).
  - [5] C. A. Schuh and A. C. Lund, Atomistic basis for the plastic yield criterion of metallic glass, *Nature Materials* **2**, 449 (2003).
  - [6] A. C. Lund, T. G. Nieh, and C. A. Schuh, Tension/compression strength asymmetry in a simulated nanocrystalline metal, *Phys. Rev. B* **69**, 012101 (2004).
  - [7] J. C. Zhang, C. Chen, Q. X. Pei, Q. Wan, W. X. Zhanga, and Z. D. Sha, Deformation and failure mechanisms of nanoscale cellular structures of metallic glasses, *RSC Adv.* **6**, 100899 (2016).
  - [8] Z. W. Shan, J. Li, Y. Q. Cheng, A. M. Minor, S. A. Syed Asif, O. L. Warren, and E. Ma, Plastic flow and failure resistance of metallic glass: Insight from in situ compression of nanopillars, *Phys. Rev. B* **77**, 155419 (2008).
  - [9] C. A. Volkert, A. Donohue, and F. Spaepen, Effect of sample size on deformation in amorphous metals, *J. Appl. Phys.* **103**, 083539 (2008).
  - [10] C. Q. Chen, Y. T. Pei, J. T. M. De Hosson, Effects of size on the mechanical response

- of metallic glasses investigated through in situ TEM bending and compression experiments, *Acta Mater.* **58**, 189 (2010).
- [11] D. Jang, C. T. Gross, J. R. Greer, Effects of size on the strength and deformation mechanism in Zr-based metallic glasses, *Int. J. Plast.* **27**, 858 (2011).
  - [12] A. Bharathula and K. M. Flores, Variability in the yield strength of a metallic glass at micron and submicron length scales, *Acta Mater.* **59**, 7199 (2011).
  - [13] O. V. Kuzmin, Y. T. Pei, and J. T. M. De Hosson, In situ compression study of taper-free metallic glass nanopillars, *Appl. Phys. Lett.* **98**, 233104 (2011).
  - [14] B.-G. Yoo, J.-Y. Kim, Y.-J. Kim, I.-C. Choi, S. Shim, T. Y. Tsui, H. Bei, U. Ramamurty, and J. Jang, Increased time-dependent room temperature plasticity in metallic glass nanopillars and its size-dependency, *Int. J. Plast.* **37**, 108 (2012).
  - [15] R. Lacroix, G. Kermouche, J. Teisseire, and E. Barthel, Plastic deformation and residual stresses in amorphous silica pillars under uniaxial loading, *Acta Mater.* **60**, 5555 (2012).
  - [16] V. Testard, L. Berthier, and W. Kob, Influence of the glass transition on the liquid-gas spinodal decomposition, *Phys. Rev. Lett.* **106**, 125702 (2011).
  - [17] V. Testard, L. Berthier, and W. Kob, Intermittent dynamics and logarithmic domain growth during the spinodal decomposition of a glass-forming liquid, *J. Chem. Phys.* **140**, 164502 (2014).
  - [18] M. A. Makeev and N. V. Priezjev, Distributions of pore sizes and atomic densities in binary glasses revealed by molecular dynamics simulations, in review (2017). (arXiv:1711.01689).
  - [19] N. V. Priezjev and M. A. Makeev, Evolution of the pore size distribution in sheared binary glasses, *Phys. Rev. E* **96**, 053004 (2017).
  - [20] N. V. Priezjev and M. A. Makeev, Structural transformations in porous glasses under mechanical loading. I. Tension, *J. Non-Cryst. Solids*, in review (2018). (arXiv:1712.04858).
  - [21] A. V. Manoylov, F. M. Borodich, and H. P. Evans, Modelling of elastic properties of sintered porous materials, *Proc. R. Soc. A* **469**, 20120689 (2013).
  - [22] W. Kob and H. C. Andersen, Testing mode-coupling theory for a supercooled binary Lennard-Jones mixture: The van Hove correlation function, *Phys. Rev. E* **51**, 4626 (1995).
  - [23] S. J. Plimpton, Fast parallel algorithms for short-range molecular dynamics, *J. Comp. Phys.* **117**, 1 (1995).
  - [24] D. Frenkel and B. Smit, *Understanding Molecular Simulation* (Academic Press, San Diego,

- 2002).
- [25] R. L. Martin, B. Smit, and M. Haranczyk, Addressing challenges of identifying geometrically diverse sets of crystalline porous materials, *J. Chem. Inf. Model.* **52**, 308 (2012).
  - [26] T. F. Willems, C. H. Rycroft, M. Kazi, J. C. Meza, and M. Haranczyk, Algorithms and tools for high-throughput geometry-based analysis of crystalline porous materials, *Micropor. Mesopor. Mater.* **149**, 134 (2012).
  - [27] D. Ongari, P. G. Boyd, S. Barthel, M. Witman, M. Haranczyk, and B. Smit, Accurate characterization of the pore volume in microporous crystalline materials, *Langmuir* (2017). (10.1021/acs.langmuir.7b01682).
  - [28] E. W. Dijkstra, A note on two problems in connexion with graphs, *Numerische Mathematik* **1**, 269 (1959).
  - [29] G. A. Simons and H. H. Legnern, An analytic model for the shock Hugoniot in porous materials, *J. Appl. Phys.* **53**, 943 (1982).
  - [30] R. F. Trunin, G. V. Simakov, Yu. N. Sutulov, A. B. Medvedev, B. D. Rogozkin, and Yu. E. Fedorov, Compressibility of porous metals in shock waves, *Sov. Phys. JETP* **69**, 580 (1989).
  - [31] M. A. Makeev, S. Sundaresh, and D. Srivastava, Shock-wave propagation through pristine *a*-SiC and carbon-nanotube-reinforced *a*-SiC matrix composites, *J. Appl. Phys.* **106**, 014311 (2009).
  - [32] L. Soulard, N. Pineau, J. Clerouin, and L. Colombet, Molecular dynamics simulations of shock compressed heterogeneous materials. I. The porous case, *J. Appl. Phys.* **117**, 115901 (2015).
  - [33] Z. Shi, P. G. Debenedetti, F. H. Stillinger, and P. Ginart, Structure, dynamics, and thermodynamics of a family of potentials with tunable softness, *J. Chem. Phys.* **135**, 084513 (2011).
  - [34] G. Y. Gor, P. Huber, and N. Bernstein, Adsorption-induced deformation of nanoporous materials—A review, *Appl. Phys. Rev.* **4**, 011303 (2017).



## Figures

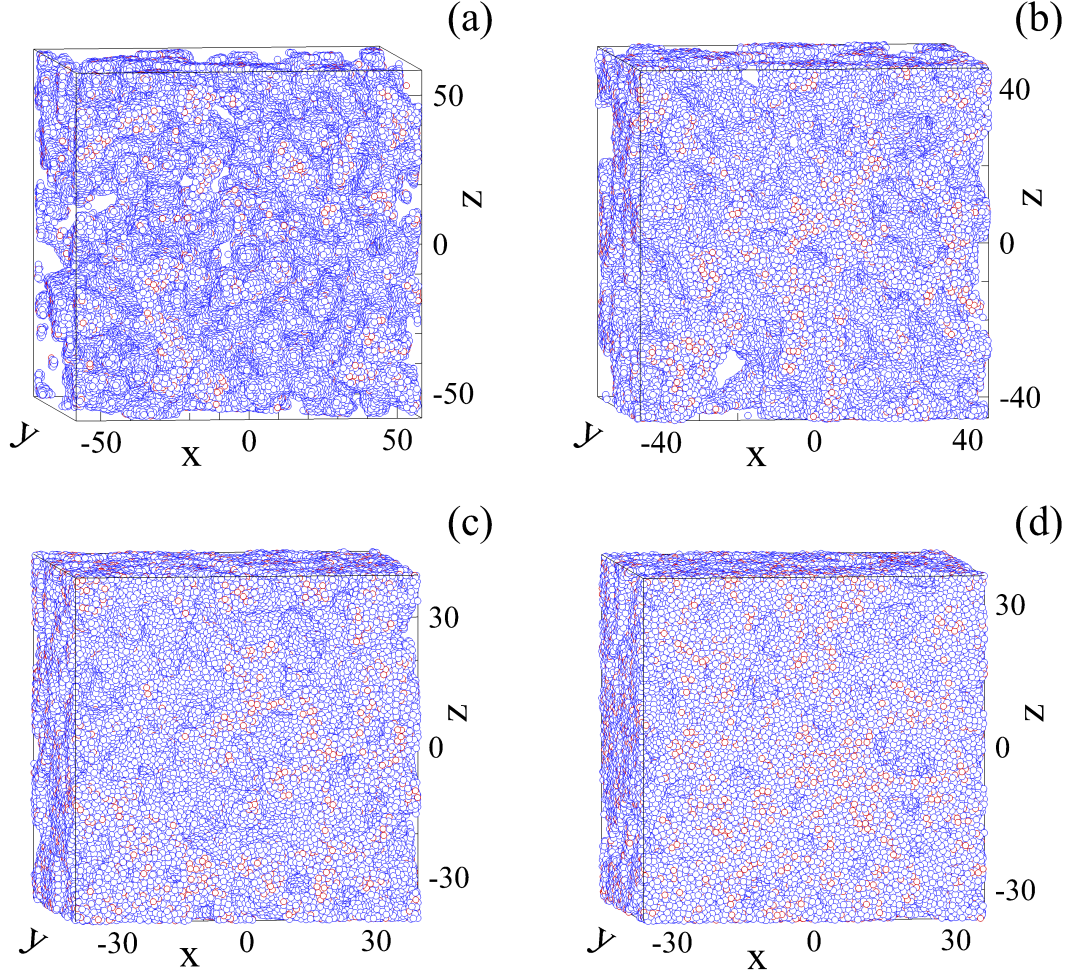


FIG. 1: (Color online) The representative snapshots of the porous samples with  $N = 300\,000$  atoms at the temperature  $T = 0.05 \varepsilon/k_B$  for the average glass densities (a)  $\rho\sigma^3 = 0.2$ , (b)  $\rho\sigma^3 = 0.4$ , (c)  $\rho\sigma^3 = 0.6$ , and (d)  $\rho\sigma^3 = 0.8$ . Different atom types are denoted by blue and red circles. Note that atoms are not depicted to scale.

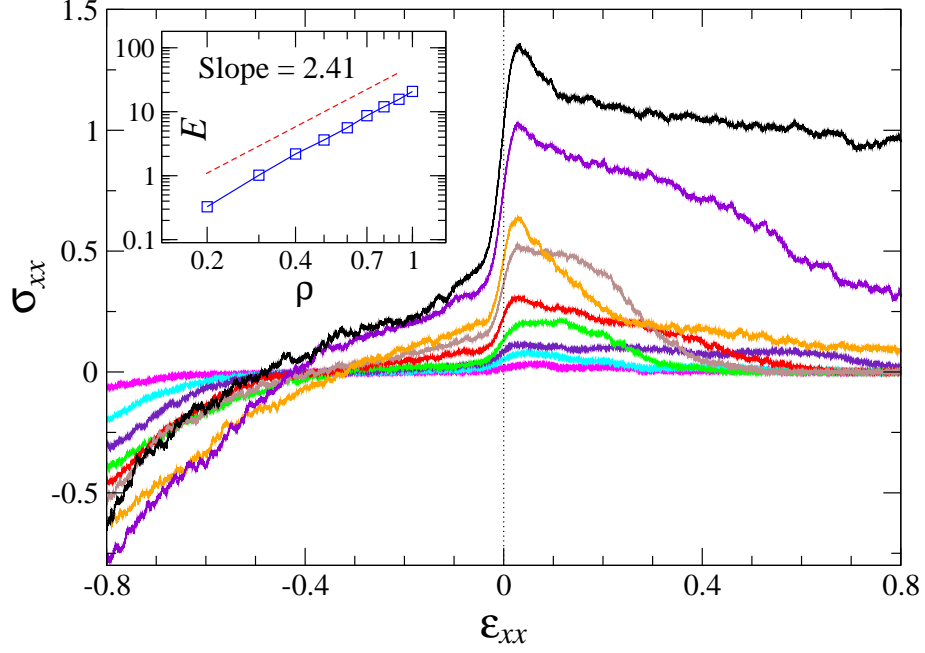


FIG. 2: (Color online) The strain dependence of stress  $\sigma_{xx}$  (in units of  $\varepsilon\sigma^{-3}$ ) during compression ( $\varepsilon_{xx} < 0$ ) and extension ( $\varepsilon_{xx} > 0$ ) with the strain rate  $\dot{\varepsilon}_{xx} = 10^{-4} \tau^{-1}$ . The average glass densities are  $\rho\sigma^3 = 0.2, 0.3, 0.4, 0.5, 0.6, 0.7, 0.8, 0.9$  and  $1.0$  (from bottom to top along the vertical dotted line). The elastic modulus  $E$  (in units of  $\varepsilon\sigma^{-3}$ ) as a function of  $\rho\sigma^{-3}$  is shown in the inset. The red dashed line is plotted for reference.

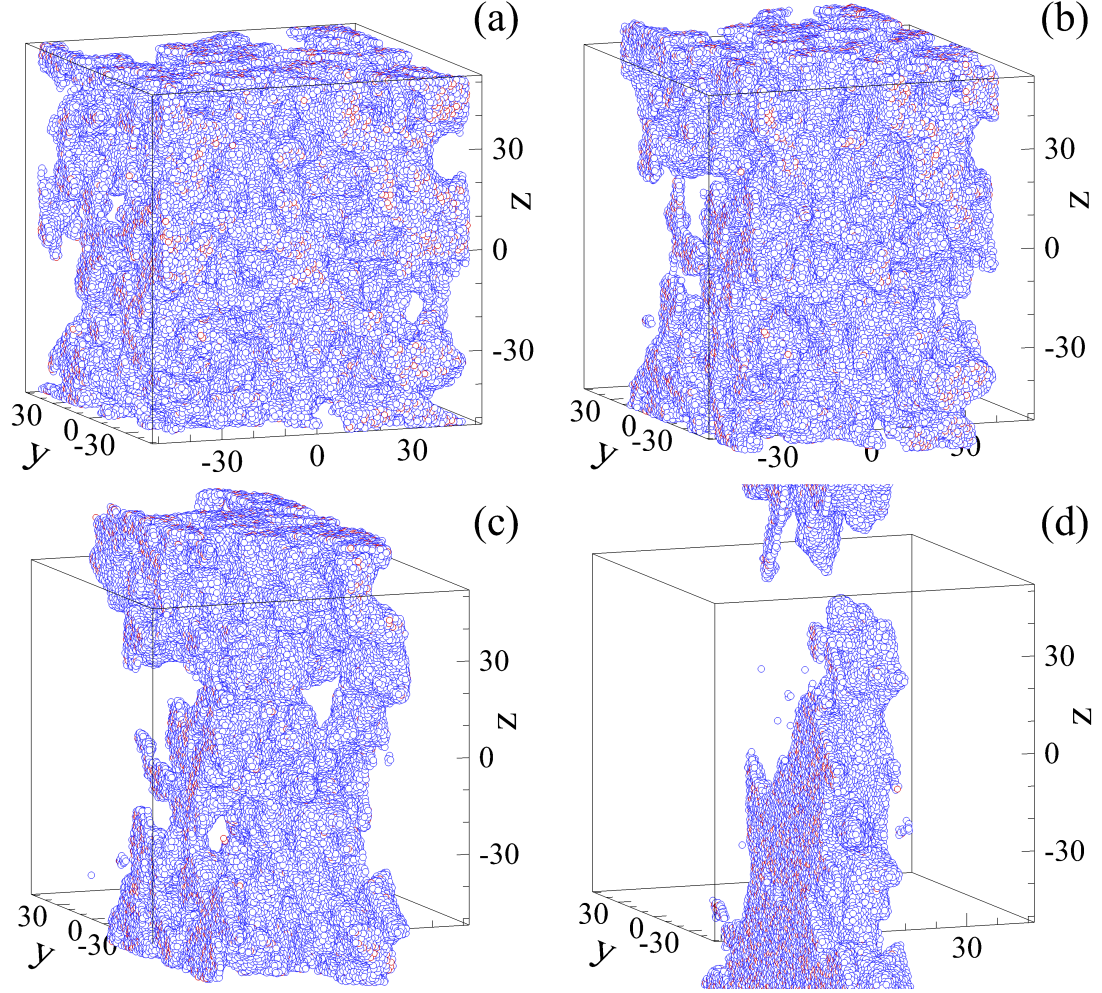


FIG. 3: (Color online) The snapshots of atomic configurations for the average glass density  $\rho\sigma^3 = 0.3$  and strain (a)  $\varepsilon_{xx} = 0.05$ , (b)  $\varepsilon_{xx} = 0.25$ , (c)  $\varepsilon_{xx} = 0.45$ , and (d)  $\varepsilon_{xx} = 0.80$ . The sample is compressed at constant volume with the strain rate  $\dot{\varepsilon}_{xx} = 10^{-4} \tau^{-1}$ .

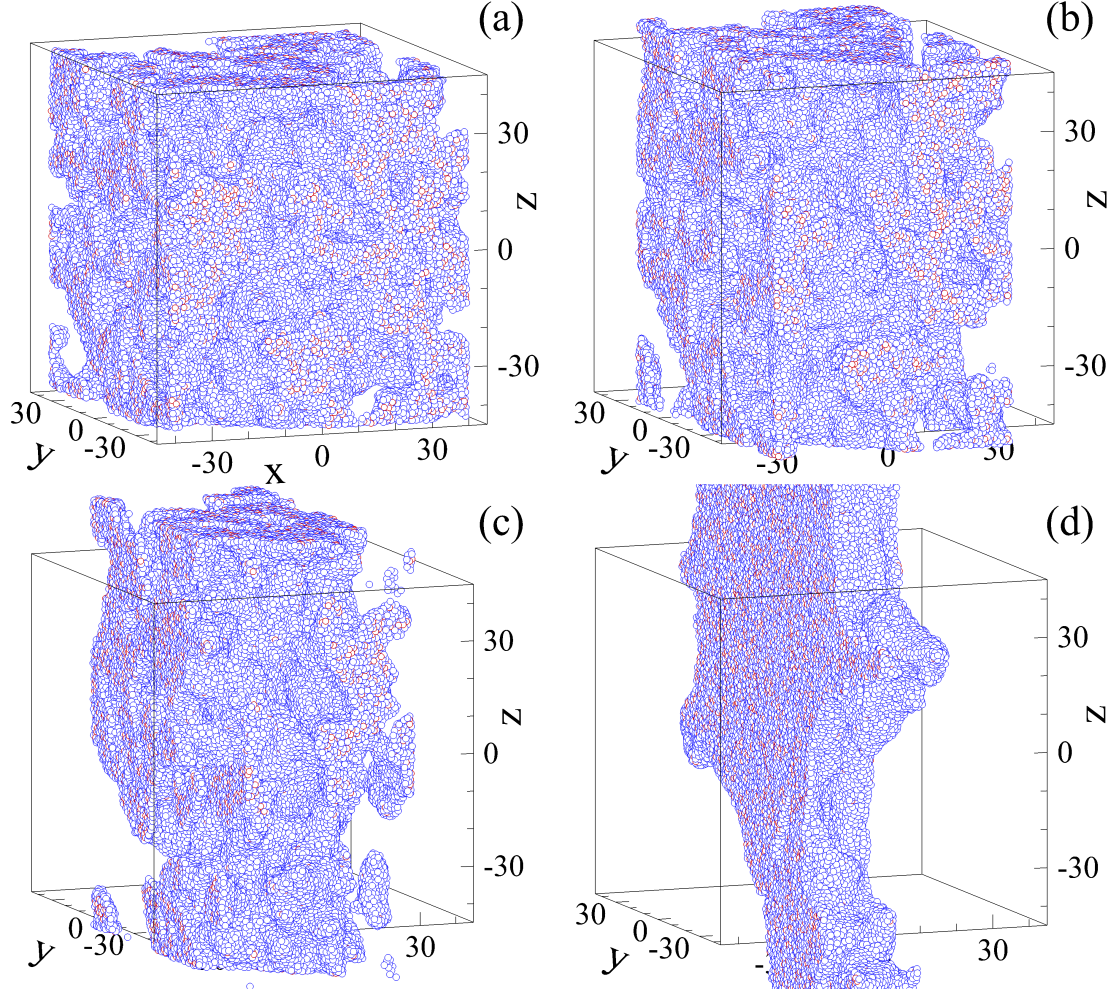


FIG. 4: (Color online) Four snapshots of the deformed porous glass with the average density  $\rho\sigma^3 = 0.5$  and strain (a)  $\varepsilon_{xx} = 0.05$ , (b)  $\varepsilon_{xx} = 0.25$ , (c)  $\varepsilon_{xx} = 0.45$ , and (d)  $\varepsilon_{xx} = 0.80$ .



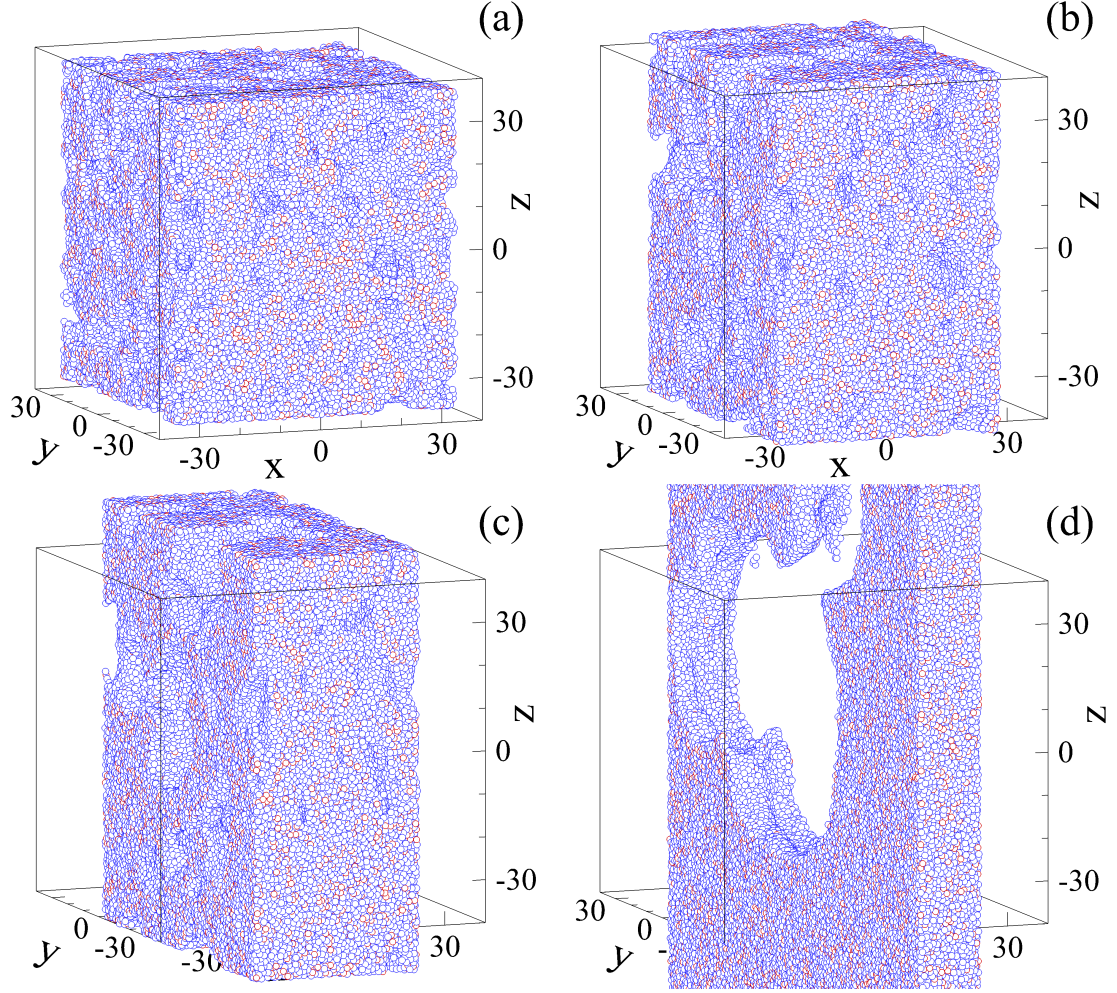


FIG. 5: (Color online) Snapshot images of the system configurations at strains (a)  $\varepsilon_{xx} = 0.05$ , (b)  $\varepsilon_{xx} = 0.25$ , (c)  $\varepsilon_{xx} = 0.45$ , and (d)  $\varepsilon_{xx} = 0.80$ . The average glass density is  $\rho\sigma^3 = 0.8$  and the strain rate is  $\dot{\varepsilon}_{xx} = 10^{-4} \tau^{-1}$ .

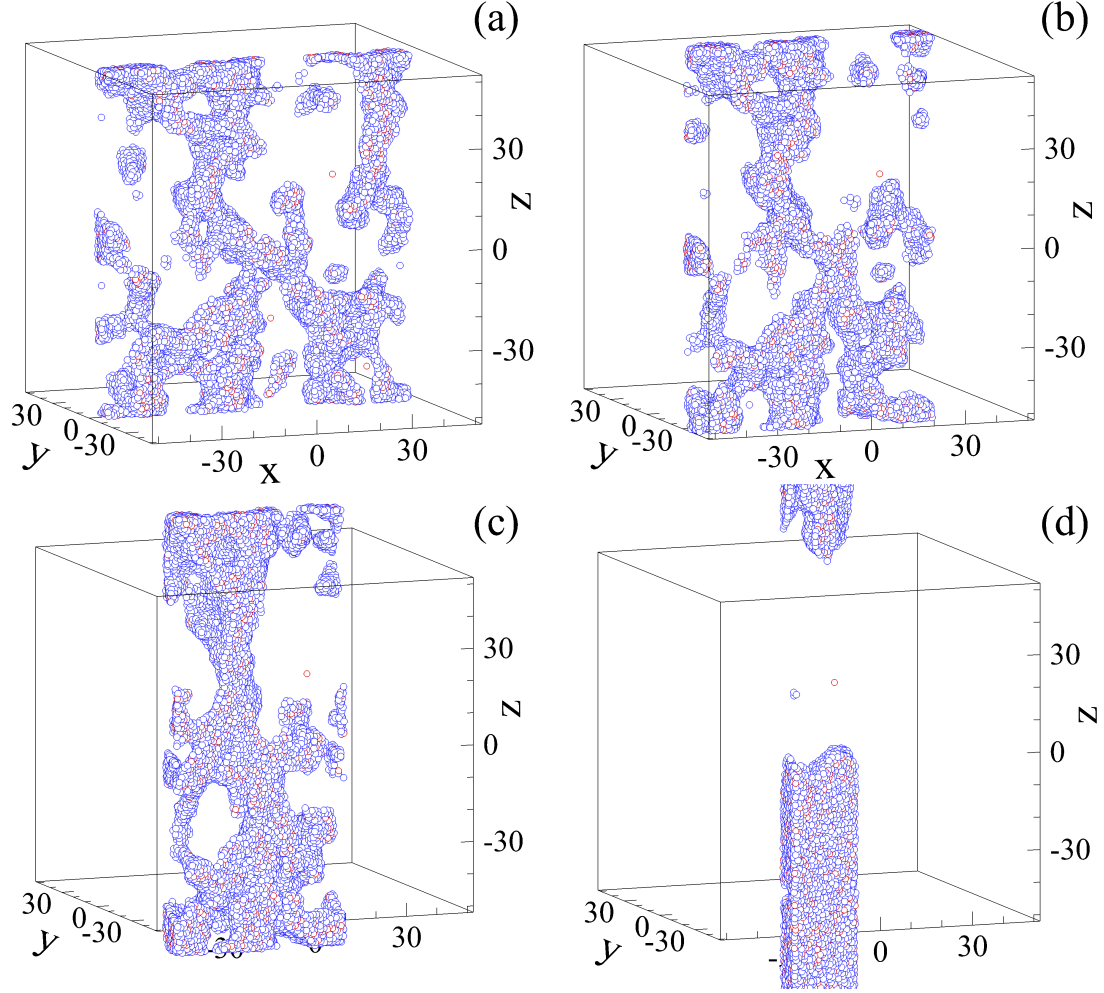


FIG. 6: (Color online) Reduced sets of data within a slice of thickness  $10\sigma$  illustrate evolution of the porous structure in the sample with the average glass density  $\rho\sigma^3 = 0.3$  and strain (a)  $\varepsilon_{xx} = 0.05$ , (b)  $\varepsilon_{xx} = 0.25$ , (c)  $\varepsilon_{xx} = 0.45$ , and (d)  $\varepsilon_{xx} = 0.80$ . The same sample as in Fig. 3.

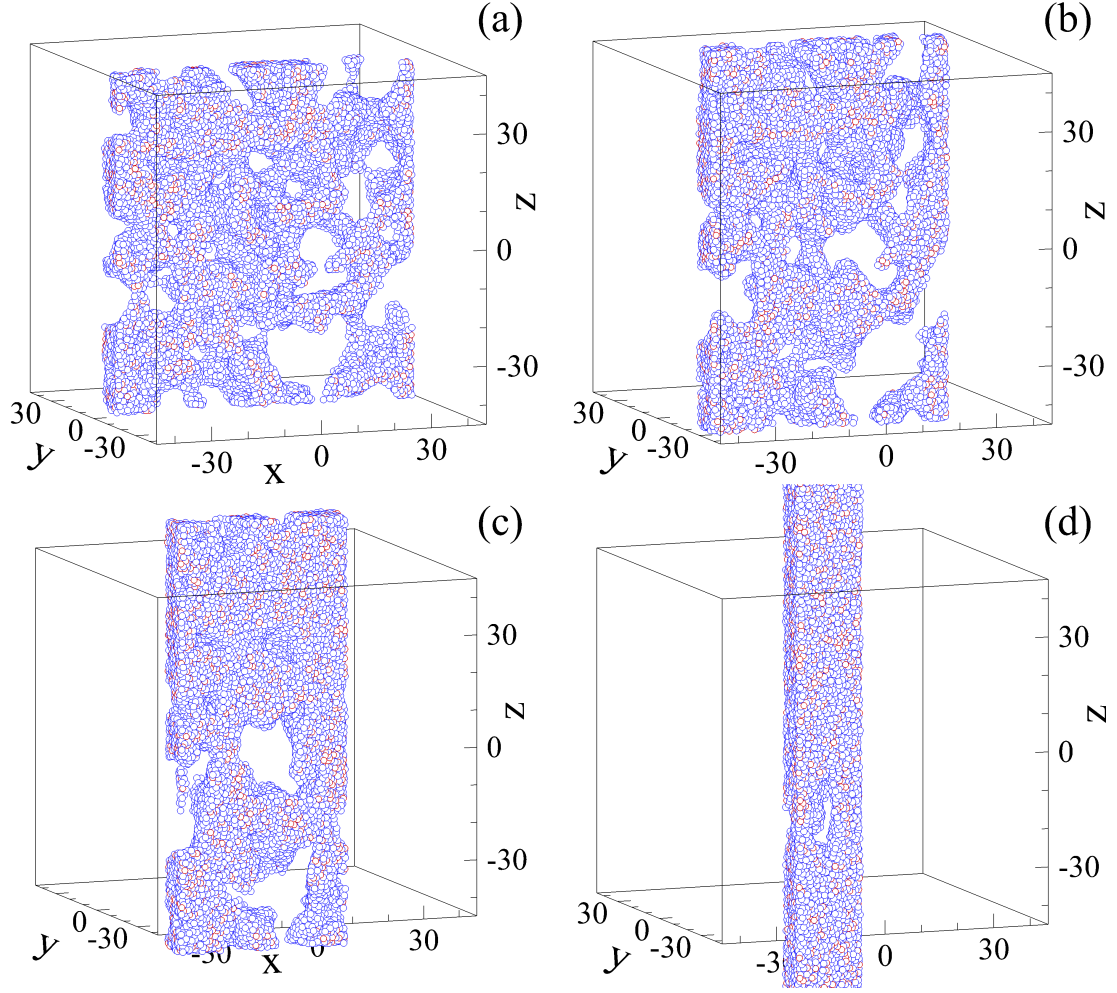


FIG. 7: (Color online) Atom configurations in a thin slice of  $10\sigma$  for the average density  $\rho\sigma^3 = 0.5$  and strain (a)  $\varepsilon_{xx} = 0.05$ , (b)  $\varepsilon_{xx} = 0.25$ , (c)  $\varepsilon_{xx} = 0.45$ , and (d)  $\varepsilon_{xx} = 0.80$ . The same sample as in Fig. 4.



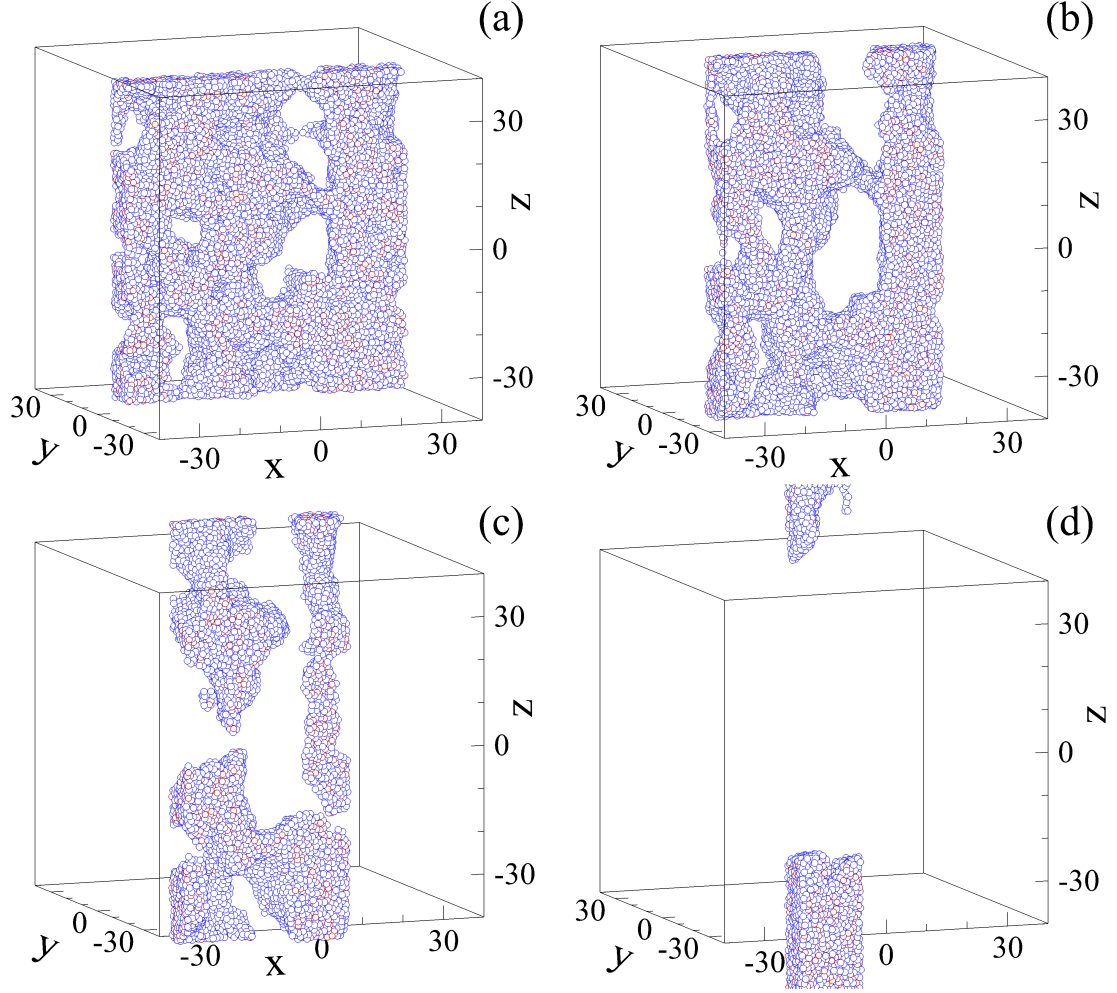


FIG. 8: (Color online) A series of snapshots of atom positions within a narrow bin with thickness of  $10\sigma$  for  $\rho\sigma^3 = 0.8$  and strain (a)  $\varepsilon_{xx} = 0.05$ , (b)  $\varepsilon_{xx} = 0.25$ , (c)  $\varepsilon_{xx} = 0.45$ , and (d)  $\varepsilon_{xx} = 0.80$ . The same sample as the one presented in Fig. 5.

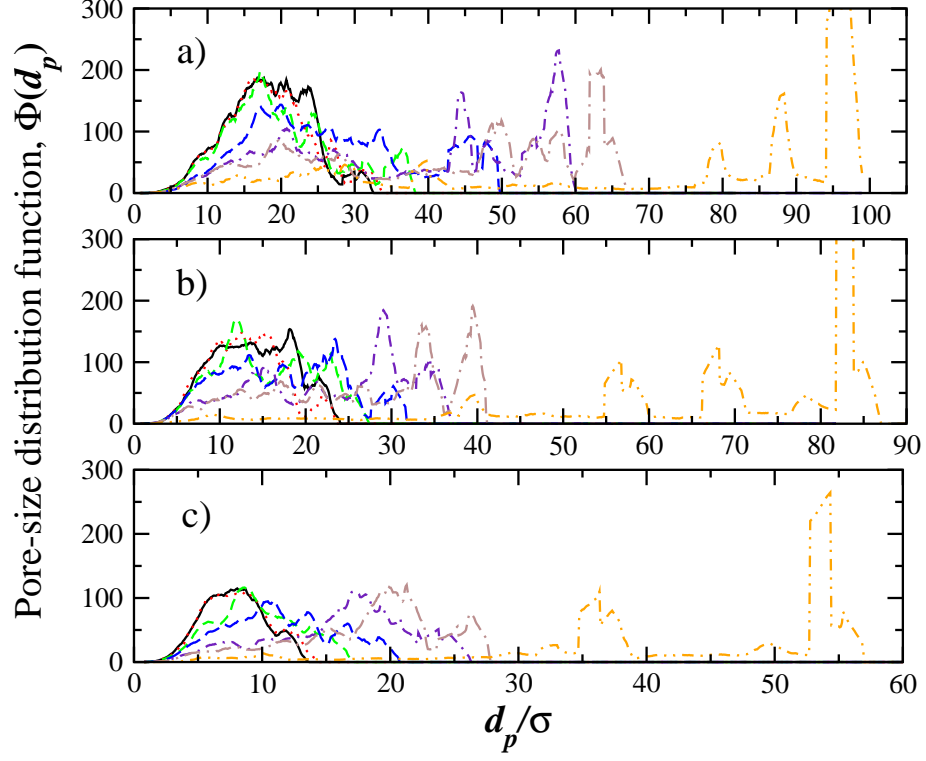


FIG. 9: (Color online) The pore size distribution functions for the cases (a)  $\rho\sigma^3 = 0.3$ , (b)  $\rho\sigma^3 = 0.5$ , and (c)  $\rho\sigma^3 = 0.8$ . The colorcode for different curves is as follow: solid black ( $\varepsilon_{xx} = 0.0$ ), dotted red ( $\varepsilon_{xx} = 0.05$ ), dashed green ( $\varepsilon_{xx} = 0.15$ ), dashed blue ( $\varepsilon_{xx} = 0.25$ ), dash-dotted indigo ( $\varepsilon_{xx} = 0.45$ ), dash-dotted brown ( $\varepsilon_{xx} = 0.50$ ), and double-dot-dashed orange ( $\varepsilon_{xx} = 0.75$ ).

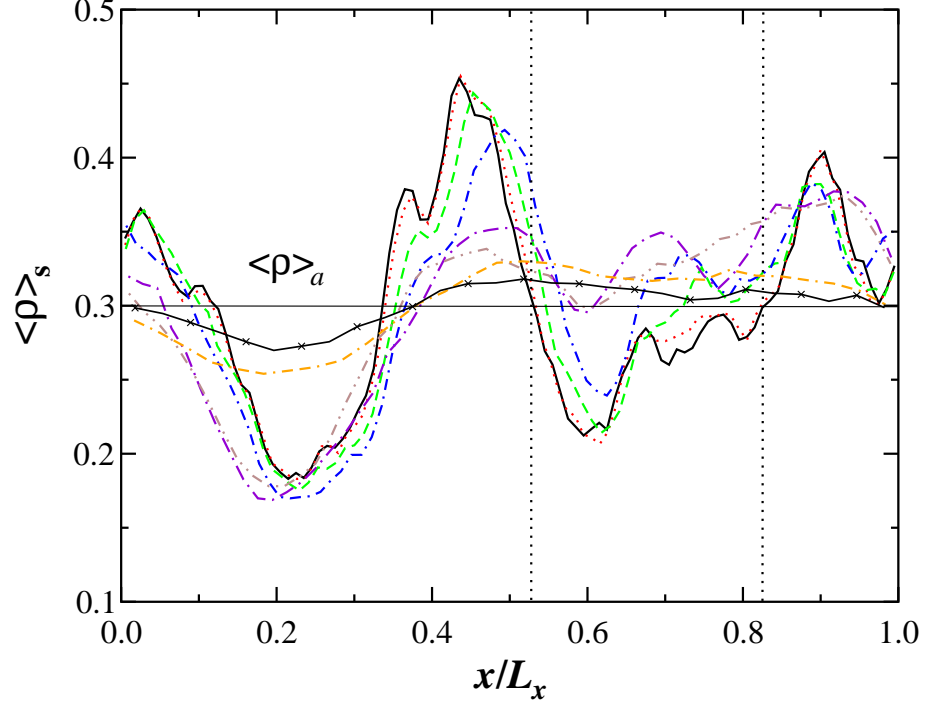


FIG. 10: (Color online) The local density profiles  $\langle \rho \rangle_s(x)$  (in units of  $\sigma^{-3}$ ) for the values of strain  $\varepsilon_{xx} = 0.0$  (solid black), 0.05 (dotted red), 0.15 (dashed green), 0.25 (dash-dotted blue), 0.45 (dash-dotted violet), 0.5 (dash-dotted brown), 0.75 (dash-dotted orange), and 0.8 (black curve with crosses). The horizontal line denotes the average glass density  $\rho\sigma^3 = 0.3$ . The two vertical dotted lines indicate the region with reduced density.

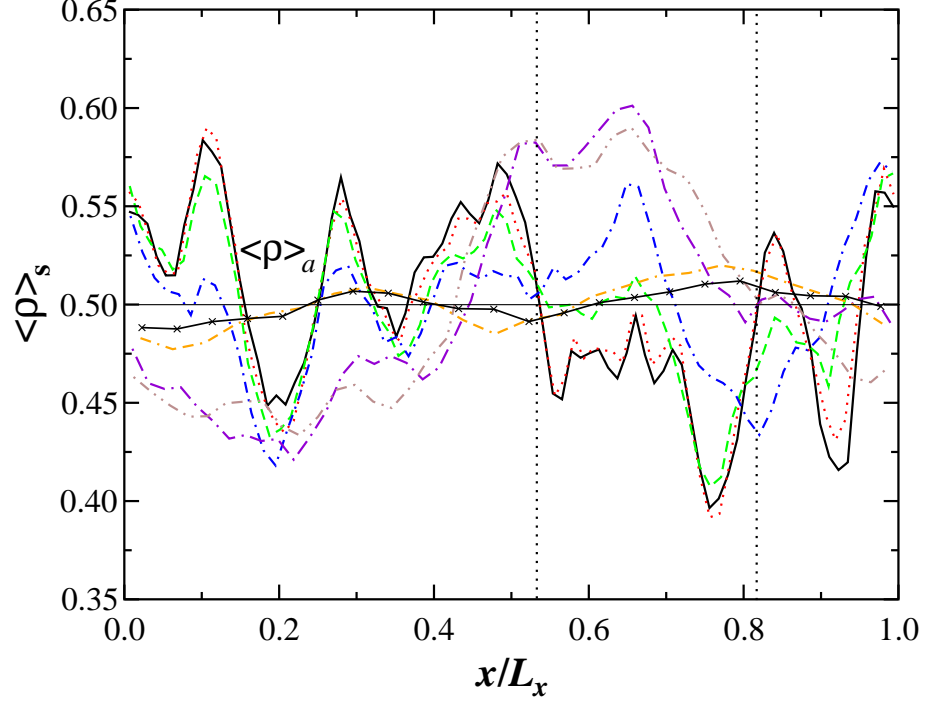


FIG. 11: (Color online) Spatially-resolved density profiles  $\langle \rho \rangle_s(x)$  (in units of  $\sigma^{-3}$ ) for the same values of compressive strain as in Fig. 10. The average glass density  $\rho\sigma^3 = 0.5$  is shown by the horizontal line. The same colorcode as in Fig. 10.

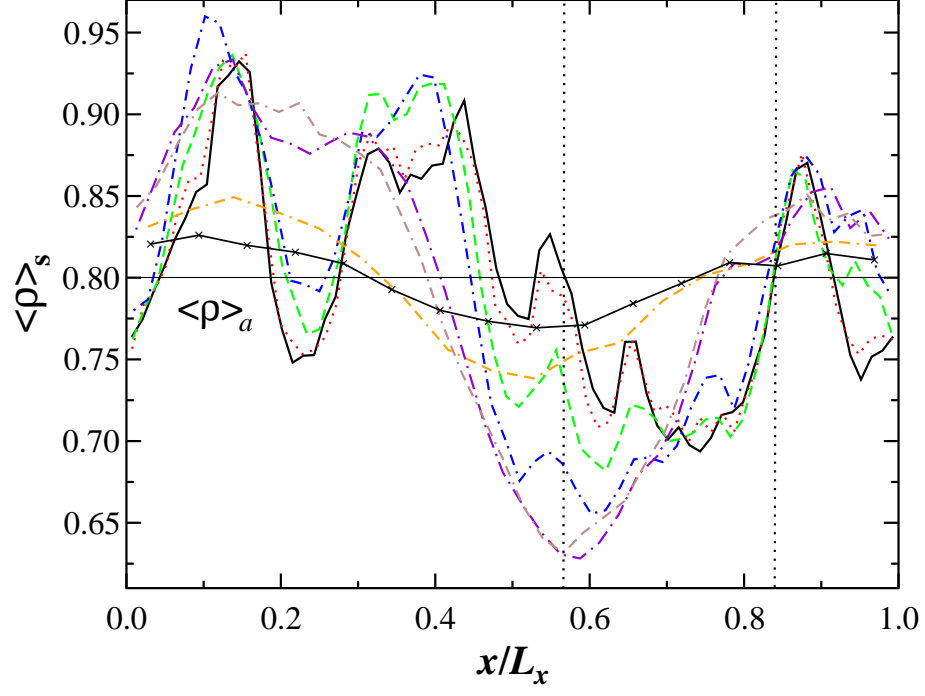


FIG. 12: (Color online) The density profiles  $\langle \rho \rangle_s(x)$  (in units of  $\sigma^{-3}$ ) of the solid phase for  $\rho\sigma^3 = 0.8$  and selected values of compressive strain. The colors and strain values are the same as in Figs. 10.